Optimal and efficient generation of sine-Gordon breathers

Xinyun Liu, Mei Wen, Xiezhi Mao, and Xinlong Wang*
Key Laboratory of Modern Acoustics (MOE) and Institute of Acoustics, Nanjing University, Nanjing 210093, P.R. China

(Received 10 January 2021; revised 7 April 2021; accepted 29 June 2021; published 14 July 2021)

We investigate analytically and numerically whether an optimally designed defect structure can significantly reduce the threshold for breather train generation by almost two orders of magnitude in a sine-Gordon chain. By optimizing the parameters of defects based on a variational approach, we show that the decoupling of in-phase and antiphase branches allows us to independently minimize the driving threshold and reach the goal of emission of high-amplitude and well-formed breathers by an ultraweak driving. These results not only provide an optimal way for highly controllable and efficient emission of breathers, but also provide some insights into the mechanism of breather excitations in such processes as the DNA-protein interaction during transcription.

DOI: 10.1103/PhysRevE.104.014209

I. INTRODUCTION

Solitonic wave objects, stable localized waves usually balanced by interplay between nonlinearity and dispersion, present one of the most striking aspects of nonlinear phenomena [1]. Although the existence, stability, and interaction of solitonic pulses have been widely investigated in recent decades, the subject of their generation in many branches of physics remains to be further explored. The creation of bright solitons in nonlinear optical fibers [2] and, recently, matter-wave solitons in Bose-Einstein condensates (BECs) [3–5] marked two milestone achievements in modern experimental and theoretical studies in this direction [6].

Controllable and efficient generation of solitonic wave trains is of particular importance in the above-mentioned and other fields, not only because it is the major player in frequency comb spectroscopy, which has revolutionized time and frequency metrology [7], but also for its application of "atom lasers" used to emit coherent atomic beams which are coherently extracted from a BEC [8,9]. Characterized by how energy is injected, trains of solitonic wave objects can be produced in several ways, namely, by preset initial conditions, imposed fields, boundary driving, etc. Controllable emission of matter waves burst from a BEC was proposed in [10], however, bearing the inherent disadvantages of amplitude decay and uneven spacing between adjacent solitary waves.

For repeated output of temporal dissipative solitons [11], a continuous wave (c.w.) is pumped into the optical cavity to compensate the resonator loss. Limited by the small temporal overlap between the ultrashort bright soliton pulse and the driving c.w. laser, the efficiency of pump-to-soliton energy conversion is typically very low. Also, controlling and stabilizing the repetition rate require sophisticated laboratory equipment. Motivated by these challenges, a recycling strategy based on coupled cavities [12] and a pulsed driving approach [13] were proposed to improve the efficiency and controllability of frequency comb generation.

Revealed by Geniet and Leon [14], supratransmission is a process by which solitonic pulse trains can be generated by periodic boundary driving in the bandgap. Most of the attention was paid exclusively to the prediction of the threshold in different systems [15–17], but adjusting the threshold, especially reducing it to a low level, is crucial for pursuing a purer waveform of solitonic pluses, as well as achieving a higher efficiency and flexibility for ultrasensitive detectors [18] and emission of solitonic pulses in a variety of applications.

Our group has proposed a scheme where solitons could be emitted periodically from a localized resonant wave induced by a mass "impurity" in the β-Fermi-Pasta-Ulam (FPU) model [19], followed recently by an experimental demonstration in a coupled pendulum chain [20]. However, an in-depth approach is still needed to develop a systematic theory for the proposed scheme, so as to explore the potential of achieving highly optimal and efficient emission of solitonic wave objects. To reach this goal, we develop the work presented here, by adopting a variational approach which makes analytical analyses possible for optimization. The results obtained by this approach are quite exciting: (1) the driving threshold is reduced by almost 2 orders of magnitude, and (2) the amplification factor, i.e., the ratio of the amplitude of solitonic pulses to the driving amplitude, can be as high as 70, whereas in our previous work [20], the ratio was only about 4. We therefore believe that the development of the present work is a big step towards understanding the mechanism of nonlinear mode excitations.

We select the sine-Gordon model in the present work to develop our theory, owing to its important applications in many branches of physics, in particular, in biological physics [21]. Some of the results revealed by this work, e.g., the extremely high efficiency of energy conversion to breathers, would provide some insights into the behaviors of DNA-protein interaction during transcription. The regulatory proteins bound to specific sites can be treated as mass [22] or coupling constant [23] defects. Previous studies mainly focus

*xlwang@nju.edu.cn

on the interaction between impurity modes and breathers which have already existed. There still exists a knowledge gap on how breathers are created from small thermal fluctuations, which is exactly the problem we deal with in this work. Our results indicate that, playing the role of large mass defects, the regulatory proteins could absorb energy from small vibrations over a wide frequency range and transfer it to high-amplitude breathers in a continuous way that is highly efficient. The emitted breathers then propagate along the DNA chain and regulate the transcription of protein binding sites downstream, which gives a complete picture of the long-range interaction effect of regulatory proteins [24]. Of course, our method is very flexible and extension to the Peyrard-Bishop model [25] is straightforward simply by modifying the Lagrangian.

II. MODEL AND FORMULATION

Here, we use the same model as in Ref. [14], except for the nonuniform mass distribution m_n, which is governed by

$$m_n\ddot{\phi}_n - c^2(\phi_{n+1} - 2\phi_n + \phi_{n-1}) + \sin\phi_n = 0, \quad n > -M, \tag{1}$$

with the boundary condition and the initial condition

$$\phi_{-M}(t) = A\sin\omega t, \quad \phi_n(0) = 0, \quad n > -M, \tag{2}$$

where A is the the driving amplitude and ω is the forcing frequency lying below the cutoff frequency, i.e., $\omega < \omega_0$ (which is scaled to 1). The coupling coefficient c in Eq. (1) is set to 4, which stands for the strong coupling condition [14]. The mass distribution m_n is given by

$$m_n = \begin{cases} m, & n = -M+1, -M+2, \ldots, 0, \\ 1, & n = 1, 2, \ldots, \end{cases} \tag{3}$$

where the positive integer M is the number of defects. The above equations can describe the dynamics of the boundary-driven Josephson transmission line [26] with junction capacitance defects and the nonlinear dynamics of the DNA-protein interaction during transcription [21,22]. If there is no defect, the system is homogeneous, i.e., $m = 1$, and in the linear approximation, it has a pass band $1 < \omega < \sqrt{1+4c^2}$.

Equation (1) could be derived from the Euler-Lagrangian equation

$$\frac{d}{dt}\frac{\partial L}{\partial\dot{\phi}_n} - \frac{\partial L}{\partial\phi_n} = 0, \tag{4}$$

where the Lagrangian is given by

$$L = \sum_{n=-M+1}^{\infty} \frac{1}{2}m_n\dot{\phi}_n^2 + c^2\left(\phi_n\phi_{n-1} - \phi_n^2\right) + \cos\phi_n - 1. \tag{5}$$

We assume that the amplitude of ϕ_n is sufficiently small that the nonlinear term can be approximated by the first two terms of the Taylor expansion, i.e., $\cos\phi_n - 1 \approx -\phi_n^2/2 + \phi_n^4/24$, so that

$$L \approx \sum_{n=-M+1}^{\infty} \frac{1}{2}m_n\dot{\phi}_n^2 + c^2\left(\phi_n\phi_{n-1} - \phi_n^2\right) - \frac{\phi_n^2}{2} + \frac{\phi_n^4}{24}. \tag{6}$$

This is the ϕ^4 model that arises in many contexts [27]. Subjected to sinusoidal boundary driving, we look for steady-state solutions in the form of $\phi_n(t) = u_n\sin\omega t$, where u_n is the amplitude of the response of the nth oscillator. Substituting it into Eq. (6) and averaging the Lagrangian over one period, $T = 2\pi/\omega$, we get the expression of the averaged Lagrangian $\mathcal{L} = \frac{1}{T}\int_0^T L dt$,

$$\mathcal{L} = \sum_{n=-M+1}^{\infty} \frac{1}{4}m_n\omega^2u_n^2 + \frac{c^2}{2}\left(u_nu_{n-1} - u_n^2\right) - \frac{u_n^2}{4} + \frac{u_n^4}{64}. \tag{7}$$

III. A SINGLE DEFECT

First, we investigate the single-defect situation, i.e., $M = 1$. Here, we assume the evanescent envelope as our ansatz,

$$u_n = \begin{cases} A, & n = -1, \\ \gamma e^{-\kappa n}, & n = 0, 1, 2, \ldots, \end{cases} \tag{8}$$

where A is the amplitude of the boundary drive, and $\kappa = 2\sinh^{-1}\sqrt{(1-\omega^2)/4c^2}$ is obtained by linearizing Eq. (1). The same treatment is also employed to obtain the interface soliton solutions in one-dimensional locally coupled lattice systems [28]. The amplitude of the evanescent wave, γ, is treated as the variational parameter in the following. Substituting our ansatz into Eq. (7) yields

$$\mathcal{L} = \frac{1}{64(1-s^{-4})}\gamma^4 + \frac{c^2A}{2}\gamma + \left[\frac{2c^2(s^{-1}-1) + \omega^2 - 1}{4(1-s^{-2})} + \frac{\omega^2(m-1)}{4}\right]\gamma^2, \tag{9}$$

where $s = e^{\kappa} > 1$. Applying the Euler-Lagrangian equation $\partial\mathcal{L}/\partial\gamma = 0$, a cubic relation between the driven amplitude A and the amplitude γ of the evanescent wave is obtained,

$$A = -\alpha\gamma(\gamma^2 - \lambda), \tag{10}$$

where the coefficients are given by

$$\alpha = \frac{1}{8c^2(1-s^{-4})}, \quad \lambda = 8[1 - \omega^2 + 2c^2(1-s^{-1})](1+s^{-2}), + 8\omega^2(1-m)(1-s^{-4}). \tag{11}$$

The cubic relation, (10), enables us to investigate the existence and stability of the stationary modes. Figure 1(a) shows the bifurcation diagram for γ versus A for three values of parameter m. Due to the antisymmetry of the function $A(\gamma)$ about the origin, only the positive part of the γ axis is presented. The curves in the first quadrant represent the in-phase branches, and the antiphase branches are represented by the curves in the fourth quadrant. The term "in phase" means that there is no phase difference between the boundary driving and the defect ($A\gamma > 0$), while "antiphase" means a 180° phase difference ($A\gamma < 0$). Based on linear stability analysis [29] and direct numerical simulations, the stable and unstable branches are identified and represented in Fig. 1(a) by solid and dashed lines, respectively. At the maximum point of an in-phase branch at $A = A_{\text{th}}^{+}$ in the first quadrant, there occurs a typical bifurcation, and stable and unstable in-phase branches collide and annihilate each other. This bifurcation

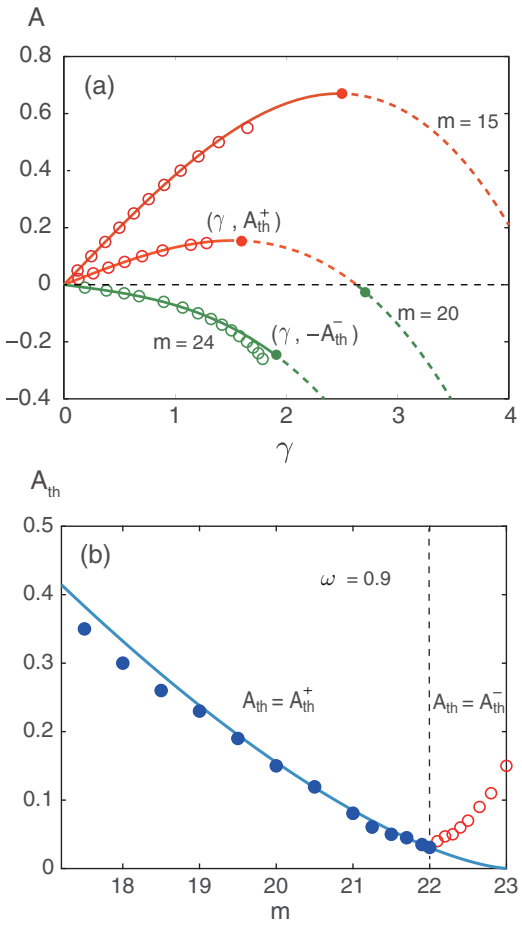

FIG. 1. (a) Dependence of the amplitude A of the drive on the amplitude γ of the evanescent wave for different m's at $\omega = 0.9$. The bifurcation points of the in-phase branch and antiphase branch are denoted $(\gamma, A_{\rm th}^{+})$ and $(\gamma, -A_{\rm th}^{-})$, respectively. The solid and dashed lines show the stable and unstable branches of the solutions calculated from Eq. (10). The circles on each curve represent the results of numerical simulations, which, of course, are stable. The part of each curve absent of circles is numerically unstable. (b) Dependence of the amplitude threshold $A_{\rm th}$ for breather generation on the mass m of the defect at $\omega = 0.9$. The solid line represents the theoretical predictions of $A_{\rm th}^{+}$ calculated from Eq. (12). The results of numerical simulations are shown by small filled and open circles, respectively, corresponding to the instability of the in-phase branch and the antiphase one. $A_{\rm th}$ takes the value of $A_{\rm th}^{+}$ for $m < 22$ and $A_{\rm th}^{-}$ for $m > 22$. The minimum value of the threshold for the breather generation occurs at the turning point, $m = 22$, which is slightly smaller than the predicted $m = 23$.

point $(\gamma, A_{\rm th}^{+})$ belonging to the in-phase branch can be derived by equating the derivative of Eq. (10) with respect to γ to 0,

$$(\gamma, A_{\rm th}^{+}) = \left(\sqrt{\frac{\lambda}{3}}, \frac{2\sqrt{3}}{9}\alpha\lambda^{\frac{3}{2}}\right). \tag{12}$$

For an antiphase branch, however, the bifurcation at $(\gamma, -A_{\rm th}^{-})$ where instability occurs cannot be analytically obtained as above, due to the limit of the cubic approximation. The driving threshold $A_{\rm th}$ for breather generation is the larger one of $A_{\rm th}^{+}$ and $A_{\rm th}^{-}$. For a given $m > 1$, we observe that the antiphase branch is much more unstable than the in-phase one, that is, $A_{\rm th}^{-} \ll A_{\rm th}^{+}$. Consequently, the threshold for breather generation is determined by the bifurcation of the in-phase branch, i.e., $A_{\rm th} = A_{\rm th}^{+}$, which enables us to obtain an *extremely low* threshold value $A_{\rm th}$ simply by minimizing the maximum of the function $A_{\rm th}^{+}(\lambda)$. As seen from formula (11), λ is a linear function of m with a negative slope, and hence, the optimal choice of m for a nearly vanishing threshold at which $\lambda = 0$ is given by

$$m = 1 + \frac{1}{1+s^{-1}}\frac{2c^2}{\omega^2} + \frac{1}{1-s^{-2}}\frac{1-\omega^2}{\omega^2}. \tag{13}$$

In the limit $1 - \omega^2 \ll 1$, $\kappa \propto \sqrt{1-\omega^2}$, and the third term in Eq. (13) can be omitted, so that $m \approx 1 + c^2 = 17$. For instance, for $\omega = 0.9$, it follows from formula (13) that the optimal parameter $m = 23$. The solid line in Fig. 1(b) shows the dependence of $A_{\rm th}^{+}$ on different values of the mass m of the defect, followed by the numerical simulations marked by small filled circles.

However, when $A_{\rm th}^{+}$ approaches 0 for $m > 22$, the $A_{\rm th}^{-}$ becomes comparable to, and then is greater than, $A_{\rm th}^{+}$. In this situation, the antiphase branch becomes more stable than the in-phase branch and takes over the threshold for breather generation, i.e., $A_{\rm th} = A_{\rm th}^{-}$, as represented by the open circles in Fig. 1(b). As a result, the lowest-amplitude threshold is achieved at the turning point $m = 22$, where $A_{\rm th}^{+} = A_{\rm th}^{-}$. In this way, the driving threshold can never be arbitrarily small and the optimal value of mass m is slightly smaller than the value predicted by (13), which are usually the cases for different frequencies (see Table I).

At the frequency $\omega = 0.9$, the numerical result shows that the threshold $A_{\rm th}$ of the driving amplitude A reaches its lowest value, $A_{\rm th} = 0.03$, at $m = 22$, while our theory predicts the lowest value at $m = 23$, showing a satisfactory agreement between the theoretical prediction and the numerical simulation. Compared with the $A_{\rm th}^{*} = 1.84$ for supratransmission in [14], the present approach thus achieves a reduction of the threshold $A_{\rm th}$ by almost 2 orders of magnitude. Table I shows that the optimal parameter m of the defect is well predicted by Eq. (13) at different frequencies. As reported in the table, the driving threshold is drastically reduced simply by the introduction of a properly designed defect over a wide frequency range, $\omega = 0.8$–0.95. Special attention is also paid to the effect of dissipation. A damping term $\beta\dot{u}_n$ is incorporated into the equations of the first 20 oscillators in our chain, with the damping coefficient β set to 0.05. It is shown that the dissipation only slightly increases the minimal threshold, to 0.09, with the parameter m shifted to 21 at $\omega = 0.9$, and thus it does not alter the studied nonlinear behavior.

A question naturally arises: Why can the ultralow threshold be achieved in the sine-Gordon chain but not found in the previous β-FPU model? To answer this question, we also present in Fig. 2 the bifurcation diagram of the model in [19] based on the method presented there, with x_0 being the peak position of the localized waves, A being the driving amplitude, and $\omega = 1.06$ being the driving frequency that slightly penetrates into the forbidden bandgap ($\omega > 1$). Note that now the vertical axis represents the driving magnitude, i.e., $|A|$. As a result, the antiphase branches, denoted I and II, have been folded along the x axis into the first quadrant for convenience

TABLE I. Comparison of the optimal m obtained by the variational approach and by simulations at different frequencies. The thresholds of supratransmission [14] are also listed ($A^*_{\rm th}$) for reference. The slight difference in the threshold value from that in [14] at $\omega = 0.9$ is due to the different initial conditions.

	m		$A_{\rm th}$	$A^*_{\rm th}$	
Frequency ω	Simulation	Theory	(with defect)	(supratransmission [14])	$A_{\rm th}$:$A^*_{\rm th}$
0.95	19	20	0.04	1.29	1/31
0.90	22	23	0.03	1.84	1/61
0.85	25	26	0.04	2.29	1/57
0.80	28	30	0.07	2.68	1/38

of comparison with the in-phase branches labeled III and IV. A linear perturbation analysis reveals that branch I is stable, whereas branches II and IV are always unstable. The metastable branch III, whose eigenvalues possess very small real parts, can be stabilized by a very weak damping. As shown in Fig. 2, the threshold of nonlinear instability is determined by two coupled maximum points of the curves. When we attempt to reduce the threshold of the antiphase branch, for example, decrease m from 0.85 to 0.65, the threshold of the in-phase branch increases, just like the waterbed effect. Their trade-off leads to the best choice of $m = 0.73$ where two peaks of the curves are of the same height at $A_{\rm th} = 0.46$. The simulations show that the parameters corresponding to the lowest threshold are $m = 0.71$ and $A_{\rm th} = 0.46$, which agree well with our analysis. In the case of supratransmission where $m = 1$, the antiphase branch dominates whose maximum $A^*_{\rm th}$ equals 1.44, which is about three times the threshold of the defective β-FPU chain. In the sine-Gordon model we explore in this work, however, there is only one maximum point belonging to the in-phase branch for $m \leqslant 22$. This allows us to minimize the threshold value independently by changing the value m without considering the unstable antiphase branch at the same time. In this sense, we say that the in-phase branch is decoupled from the antiphase branch, enabling a remarkable reduction of the threshold of supratransmission by almost 2 orders of magnitude.

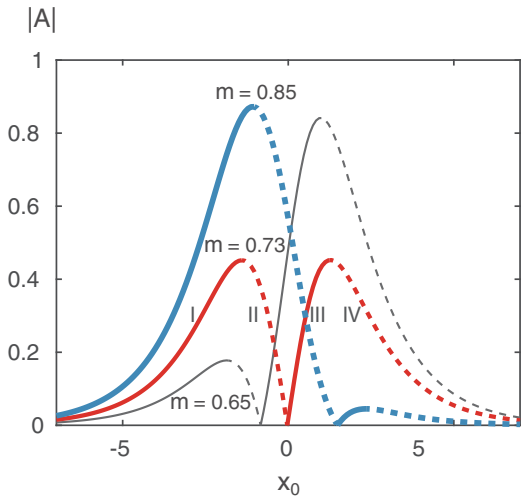

FIG. 2. Bifurcation diagram of the β-FPU model [19]. Dependence of the magnitude $|A|$ of the drive on the peak position x_0 of localized waves for $m = 0.85$ (thick blue line), 0.73 (normal red line), and 0.65 (thin gray line).

IV. EMISSION OF BREATHER TRAINS

After the investigation of nonlinear instability of the defect mode, we study in this section the potential for controllable

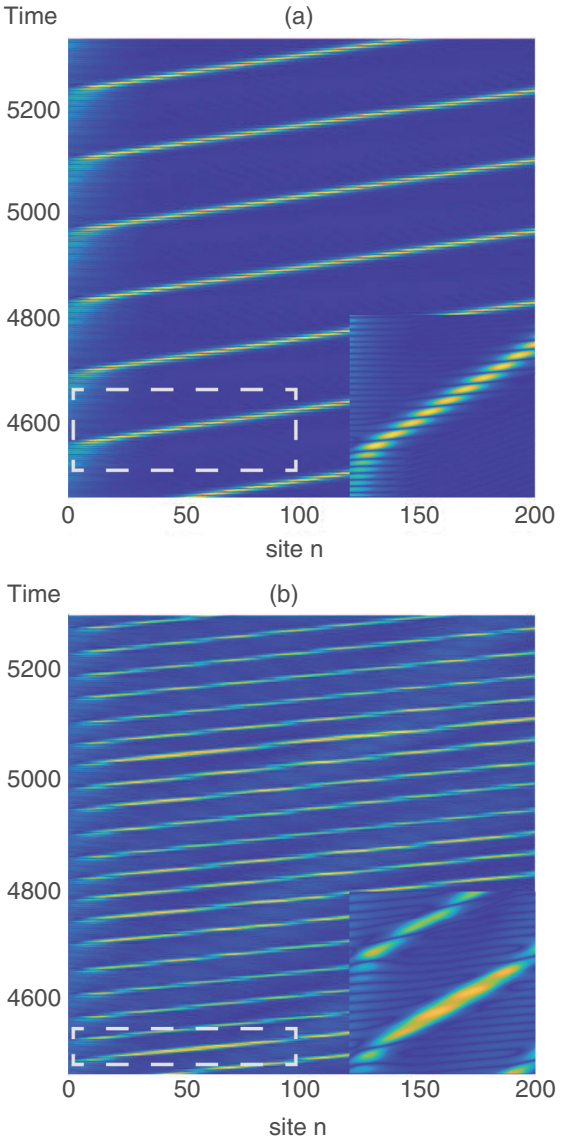

FIG. 3. Spatial-temporal evolution of wave fields for (a) $m = 22$ and (b) $m = 1$. The vertical axis in (a) and (b) is the time from $t = 4500$ to $t = 5300$ and the horizontal axis represents the first 200 oscillators. Insets: Magnified views of the boxed regions.

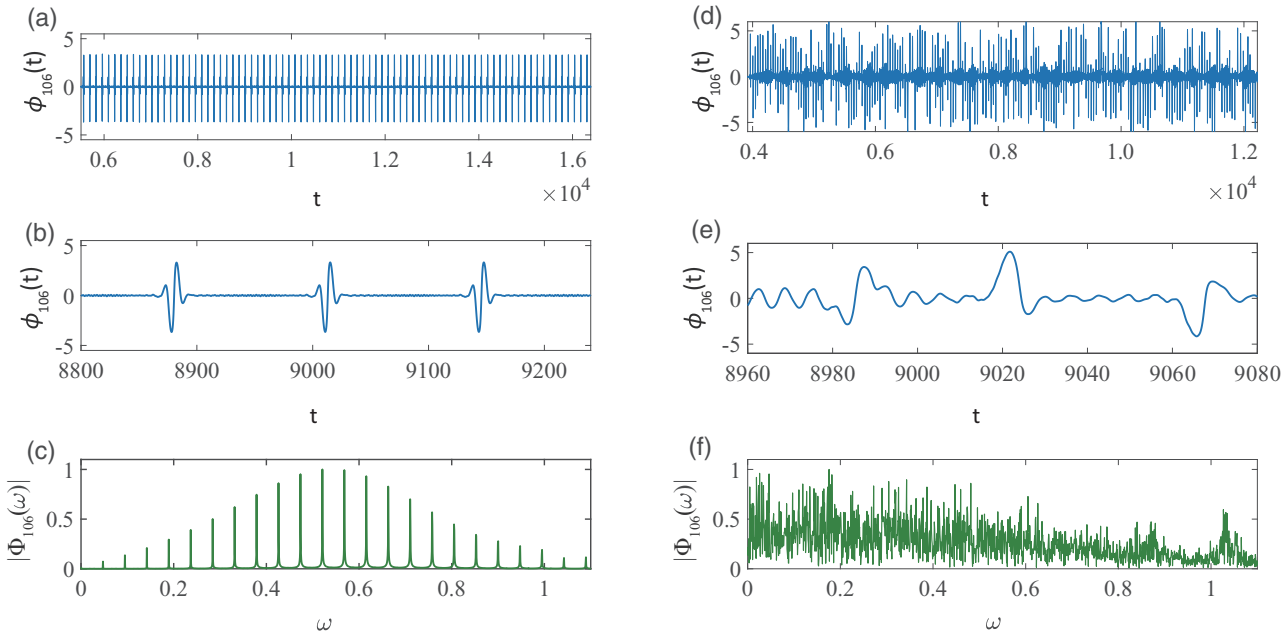

FIG. 4. (a) The time signal of ϕ_n detected at site $n = 106$, (b) its magnified view, and (c) its Fourier components $\Phi_{106}(\omega)$ with boundary driving amplitude $A = 0.06$ and frequency $\omega = 0.9$. The chain consists of a total number of 700 oscillators with a mass defect $m = 22$ at $n = 0$. (d) The time signal of ϕ_n detected at site $n = 106$, (e) its magnified view, and (f) its Fourier components $\Phi_{106}(\omega)$ for a homogeneous chain (i.e., $m = 1$) when the driving amplitude A is set to 1.84, which is the threshold value for supratransmission.

generation of breather trains, whose significance has been clarified in Sec. I. We adopt the Runge-Kutta algorithm to integrate the discrete sine-Gordon model, Eqs. (1) and (2), with a single impurity, $m_0 = 22$. The chain initially at rest consists of a total of 700 oscillators and it is forced by a boundary driving of the form $\phi_{-1} = A \sin \omega t(1 - \exp(-(t/\tau)^2))$, where $\tau = 1500$ is used to avoid the initial shock. For all simulations in this work, the damping coefficient of the last 300 units increases linearly from 0 to 0.1 to suppress the reflection from the other end.

Figures 3(a) and 3(b) show the spatial-temporal evolution of the waves for defective and homogeneous chains, respectively, at the driving frequency $\omega = 0.9$. The driving amplitude A is taken to be 0.06 for our defective model and 1.84 for the homogeneous chain, which is the driving threshold for supratransmission. As shown in Fig. 3(a), the localized mode around the defect undergoes a strong modulation on a slower time scale ($T_s = 132.6$) than the period of oscillations ($T = 2\pi/\omega \approx 7.0$). When absorbing enough energy from the weak driving, the localized wave splits out a high-amplitude breather which carries most of the localized energy away. Once generated, the moving breather of height 4.1 propagates down the chain at an unchanged speed. The insets are magnified views of the boxed portions, showing the breathing properties of the moving breathers. The periodical repetition of the emission process leads to the creation of a train of well-shaped breathers that are almost equidistantly separated. Calculated by a total of 90 data points, the mean period of emissions is $T_s = 132.6$ with a standard deviation $\sigma_s = 3.46$. Differently from optical microresonators, this period is determined by the modulation instability of the localized wave subjected to external driving and, thus, could be directly controlled by finely adjusting the driving amplitude A and frequency ω. One can see that there are no visible waves other than breathers in the far field, revealing an almost 100% efficiency of energy conversion to breathers. Another notable fact is that the amplitude of breathers reaches $A_s = 4.1$, while the driving amplitude A is merely 0.06. Defined by A_s/A, the amplification factor approaches 70, which is also an order of magnitude larger than that in [20], where the ratio is about 4. In the case of supratransmission as shown in Fig. 3(b), the seemingly irregular nonlinear pulses accompanied by the background noise are generated much more rapidly, probably due to the high driving strength, showing the disorder of the breather train and the low efficiency of energy conversion.

To see the details of the radiated wave field in the time domain, the time evolution of $\phi_{106}(t)$ under the same driving conditions as above is presented in Fig. 4(a). Spaced at an average time interval of 133, the waveforms of breathers are almost identical, as is clearly shown in the magnified view in Fig. 4(b). Using the fast Fourier transformation, the corresponding Fourier components $\Phi_{106}(\omega)$ of the time signal $\phi_{106}(t)$ recorded in Fig. 4(a) are computed and plotted in Fig. 4(c). The magnitude of the frequency components has been normalized to the one at the central frequency $\omega = 0.52$. We can see a low-noise frequency comb whose components space the whole range of the pass band at a frequency interval $\Delta\omega = 2\pi/T_s = 0.047$. In Figs. 4(d)–4(f), the results for a homogeneous sine-Gordon chain (i.e., $m = 1$) are also presented for comparison, indicating that the emitted pulses are always accompanied by the quasilinear wave background and other strong nonlinear modes with a seemingly stochastic frequency spectrum.

The drastic reduction of the driving amplitude not only significantly suppresses the undesired waves but also greatly extends the parameter space for controllable emission of

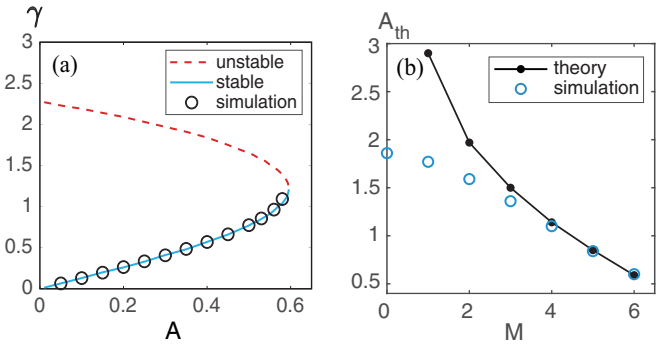

FIG. 5. (a) Dependence of γ on the driving amplitude A for $M = 6$ and $m = 2$. (b) Prediction (small filled circles) of A_{th} for different M's compared with the numerical results for $m = 2$. In both (a) and (b), circles are the data points computed numerically.

breathers, which are crucial for both experimental studies and applications. Although the driving amplitude is almost 2 orders smaller in magnitude, the heights of generated breathers are comparable to those of breathers generated via supratransmission. All these features indicate that our scheme is promising for generating superefficient breather trains and low-noise frequency combs.

V. DEFECT CAVITY

In this section we consider the case of $M > 1$, i.e., the existence of multiple identical defects, all with equal m. The defective part ($-M < n \leqslant 0$) has the cutoff frequency $\omega_c = 1/\sqrt{m}$, while the cutoff $\omega_0 = 1$ for the rest ($n > 0$). The driving frequency ω is set to be slightly below ω_0 but still greater than ω_c, so that linear waves are permitted in the defect cavity but are evanescent in the other part ($n > 0$) of the chain. In this way, the standing sinusoidal wave in the defective part, called the "defect cavity" here, couples with the evanescent wave at the boundary $n = 0$. The following linear solution of the coupled model satisfying the continuity condition is adopted as our ansatz,

$$u_n = \begin{cases} \gamma \cos kn - \eta \sin kn, & n = -M+1, \ldots, 0, \\ \gamma e^{-\kappa n}, & n = 0, 1, 2, \ldots, \end{cases} \tag{14}$$

where (γ, η) are regarded as our variational parameters, and k, the propagation constant in the defect cavity, is given by $k = 2\sin^{-1}\sqrt{(m\omega^2 - 1)/4c^2}$.

Substituting Eq. (14) into Eq. (7) and using the Euler-Lagrangian equation $\partial\mathcal{L}/\partial\gamma = 0, \partial\mathcal{L}/\partial\eta = 0$, we obtain a pair of coupled cubic equations of (γ, η), which are somewhat lengthy but can be solved numerically.

Figure 5(a) shows a typical bifurcation diagram for the defect cavity, which is obtained for $M = 6$ and $m = 2$. Being the response amplitude at the interface ($n = 0$), the parameter γ monotonically increases with the driving amplitude A along the stable branch, which collides with the unstable one at $A = 0.59$ and then vanishes. The stable stationary solutions are validated by direct simulations represented by circles. It was shown that the value of A at the bifurcation point corresponds to the onset of the nonlinear instability A_{th}, leading to the generation of nonlinear modes propagating down the chain. Figure 5(b) plots the prediction of the driving threshold A_{th} for different cavity lengths M. Simulation results agree quite well with the theoretical prediction in the low-amplitude region, while for large values of A_{th} our approximation becomes inaccurate. In the case of short cavities, for example, $M = 1$ and $m = 2$, the amplitude of localized waves near the

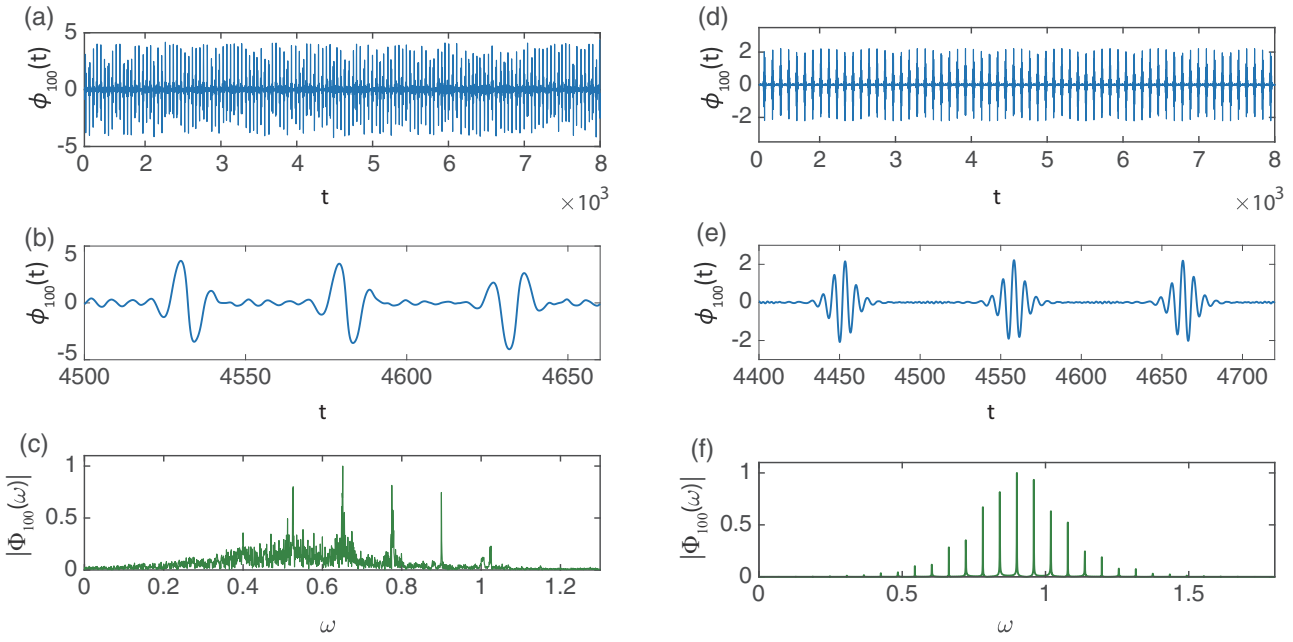

FIG. 6. (a) The time signal of ϕ_n detected at site $n = 100$, (b) its magnified view, and (c) its Fourier components $\Phi_{100}(\omega)$ detected at site $n = 100$ with a boundary driving amplitude $A = 0.62$ and frequency $\omega = 0.9$. (d) The time signal of ϕ_n detected at site $n = 100$, (e) its magnified view, and (f) its Fourier components $\Phi_{100}(\omega)$ under the same conditions except for the additionally incorporated damping term $\beta\dot{u}_n$ on the left-hand side of Eq. (1) of the first 20 oscillators.

onset of instability is so high that the cubic approximation in our model is no longer valid. Our investigation shows that for $M > 6$, the nonlinear behaviors in the defect cavity are quite different, and when M approaches 10, linear resonance occurs in the defect cavity. Consequently, the localized waves undergo a strong modulation instead and radiate little energy to the far field, which is not the scope of this research.

Figure 6(a) shows the time evolution of the oscillation at site $n = 100$, and Fig. 6(b) is a magnified portion of the signal. Since the driving amplitude here is 10 times as large as that of a single defect, other nonlinear modes and a quasilinear wave background are also generated, accompanied by the traveling breathers and corrupting the spectrum as shown in Fig. 6(c). An attempt is made to take into account the effect of weak dissipation to suppress these undesired waves. As demonstrated in [30], the dissipation effect sometimes benefits the periodic production of propagating solitons. Hence the damping term $\beta \dot{u}_n$ is incorporated in the governing equations, (1), for the first 20 oscillators near the driving, here with the damping coefficient β set to 0.05. Simulations are performed under the same other conditions as stated above. Now a train of "clean" breathers is emitted in a long time span, as shown in Figs. 6(d) and 6(e). It should be noted that the modulation of the train's envelope, as shown in Fig. 6(d), *does not* mean variation of the breathers' amplitude, but indicates a phase shift between successive breathers arriving at $n = 100$, due to the inherent properties of moving breathers. Again the "clean" moving breathers give a comblike spectrum, as shown in Fig. 6(f), where such unwanted components as in Fig. 6(c) are successfully suppressed. Of course, the damping dissipation has the side effect of shifting the central frequency of the comb to $\omega = 0.9$.

VI. CONCLUSION

We have achieved the highly efficient and controllable emission of trains of breathers by a boundary driver of ultralow driving threshold in defective sine-Gordon chains. The efficiency is achieved by optimization of the parameters of the properly designed defects via the variational approach. The emitted pulse train consists of a series of high-amplitude, well-shaped, and equidistant breathers, enabling the generation of low-noise frequency combs in frequency space. By the advantage of an ultralow driving amplitude, the flexibility and efficiency for breather excitation can be greatly improved without affecting the amplitude of breathers. Moreover, this gives a reasonable explanation for the breather excitation from small thermal vibrations in the process of transcription [21–24]. Applying this scheme to continuous systems will be the focus of our further work, which we believe could provide some insights into the related issues in nonlinear optics, BECs, and other important fields of physics.

ACKNOWLEDGMENTS

This work was supported by the National Science Foundation of China under Grant Nos. 11574149 and 10874085.

[1] M. Remoissenet, *Waves Called Solitons: Concepts and Experiments* (Springer-Verlag, New York, 1999).
[2] L. F. Mollenauer, R. H. Stolen, and J. P. Gordon, Phys. Rev. Lett. **45**, 1095 (1980).
[3] S. Burger, K. Bongs, S. Dettmer, W. Ertmer, K. Sengstock, A. Sanpera, G. V. Shlyapnikov, and M. Lewenstein, Phys. Rev. Lett. **83**, 5198 (1999).
[4] L. Khaykovich, F. Schreck, G. Ferrari, T. Bourdel, J. Cubizolles, L. D. Carr, Y. Castin, and C. Salomon, Science **296**, 1290 (2002).
[5] K. E. Strecker, G. B. Partridge, A. G. Truscott, and R. G. Hulet, Nature (London) **417**, 150 (2002).
[6] Y. V. Kartashov, B. A. Malomed, and L. Torner, Rev. Mod. Phys. **83**, 247 (2011).
[7] N. Picqué and T. W. Hänsch, Nat. Photon. **13**, 146 (2019).
[8] I. Bloch, T. W. Hänsch, and T. Esslinger, Phys. Rev. Lett. **82**, 3008 (1999).
[9] A. Öttl, S. Ritter, M. Köhl, and T. Esslinger, Phys. Rev. Lett. **95**, 090404 (2005).
[10] M. I. Rodas-Verde, H. Michinel, and V. M. Pérez-García, Phys. Rev. Lett. **95**, 153903 (2005).
[11] T. Herr, V. Brasch, J. D. Jost, C. Y. Wang, N. M. Kondratiev, M. L. Gorodetsky, and T. J. Kippenberg, Nat. Photon. **8**, 145 (2014).
[12] X. Xue, X. Zheng, and B. Zhou, Nat. Photon. **13**, 616 (2019).
[13] E. Obrzud, S. Lecomte, and T. Herr, Nat. Photon. **11**, 600 (2017).
[14] F. Geniet and J. Leon, Phys. Rev. Lett. **89**, 134102 (2002).
[15] R. Khomeriki, S. Lepri, and S. Ruffo, Phys. Rev. E **70**, 066626 (2004).
[16] R. Khomeriki, Phys. Rev. Lett. **92**, 063905 (2004).
[17] P. Anghel-Vasilescu, J. Dorignac, F. Geniet, J. Leon, and M. Taki, Phys. Rev. Lett. **105**, 074101 (2010).
[18] D. Chevriaux, R. Khomeriki, and J. Leon, Phys. Rev. B **73**, 214516 (2006).
[19] G. Yu, X. Wang, and Z. Tao, Phys. Rev. E **83**, 026605 (2011).
[20] X. Liu, X. Wang, H. Liu, S. Wang, and M. Wen, Phys. Rev. E **102**, 052201 (2020).
[21] M. Salerno and Yu.S. Kivshar, Phys. Lett. A **193**, 263 (1994).
[22] K. Forinash, M. Peyrard, and B. Malomed, Phys. Rev. E **49**, 3400 (1994).
[23] J. J.-L. Ting and M. Peyrard, Phys. Rev. E **53**, 1011 (1996).
[24] M. V. Satarić and J. A. Tuszyński, Phys. Rev. E **65**, 051901 (2002).
[25] M. Peyrard and A. R. Bishop, Phys. Rev. Lett. **62**, 2755 (1989).
[26] R. Khomeriki and J. Leon, J. Phys.: Conf. Ser. **150**, 022035 (2009).
[27] Y. M. Shnir, *Topological and Non-Topological Solitons in Scalar Field Theories* (Cambridge University Press, Cambridge, UK, 2018).
[28] L. Hadžievski, G. Gligorić, A. Maluckov, and B. A. Malomed, Phys. Rev. A **82**, 033806 (2010).
[29] K. W. Sandusky, J. B. Page, and K. E. Schmidt, Phys. Rev. B **46**, 6161 (1992).
[30] E. Kit, L. Shemer, and T. Miloh, J. Fluid Mech. **181**, 265 (1987).